# Supplementary Material:

Layered 3D: Tomographic Image Synthesis for Attenuation-based Light Field and High Dynamic Range Displays

Gordon Wetzstein[1]   Douglas Lanman[2]   Wolfgang Heidrich[1]   Ramesh Raskar[2]

[1]University of British Columbia   [2]MIT Media Lab

This document contains additional results, analysis, and extended derivations in support of the primary text. Appendix A includes high-resolution images of the prototype. Appendices B and C further document 3D display and HDR imaging, respectively. Appendix D summarizes optimization of display parameters depending on target light field content. Finally, Appendix E provides an extended analysis of depth of field for multi-layer displays.

## A   High-Resolution Images of the Multi-Layer Display Prototype
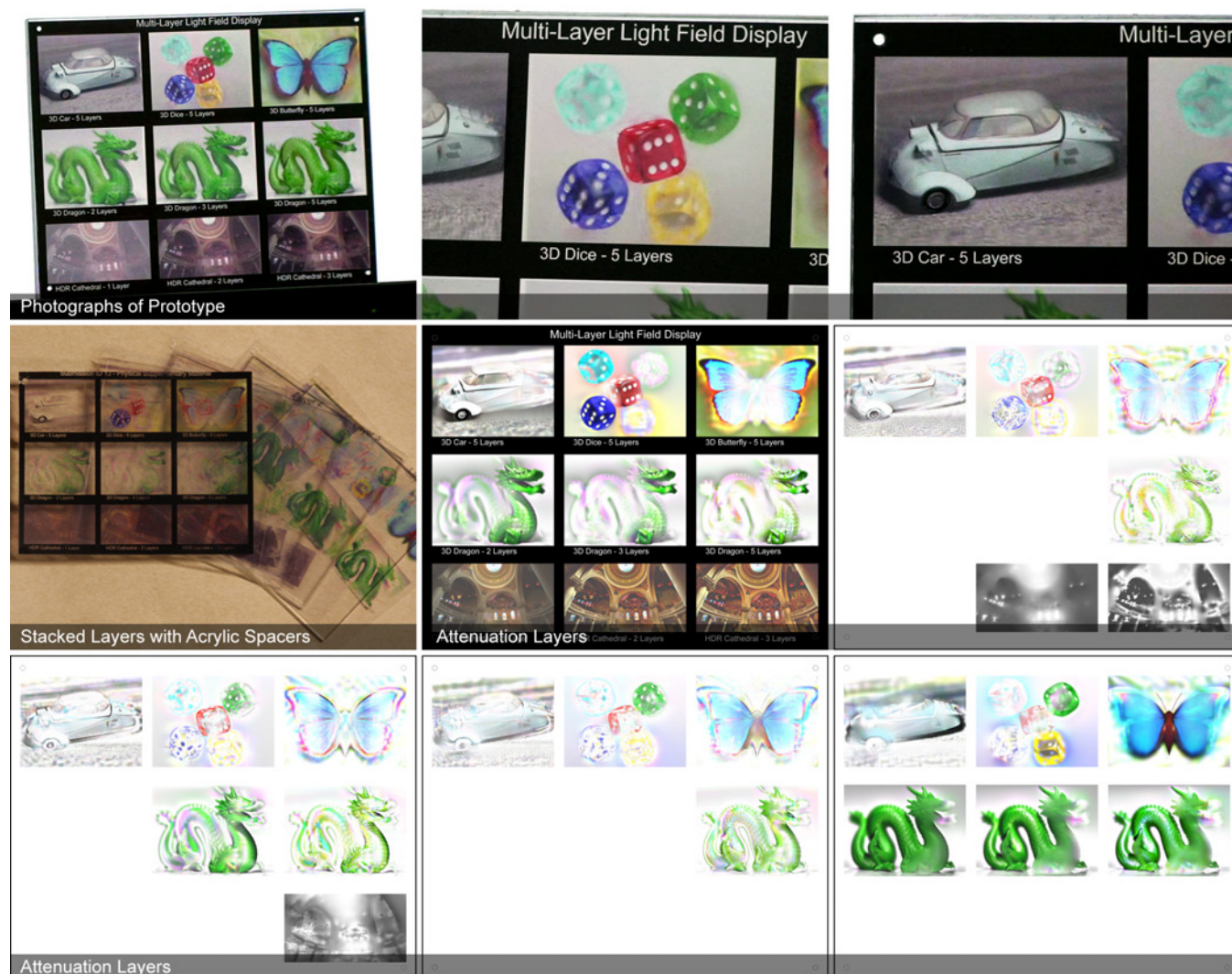
Figure S.1: *Additional photographs of one of the display prototypes (top row), along with the individual attenuation layers (center and bottom rows).*

B   Additional Results for 3D Image Display
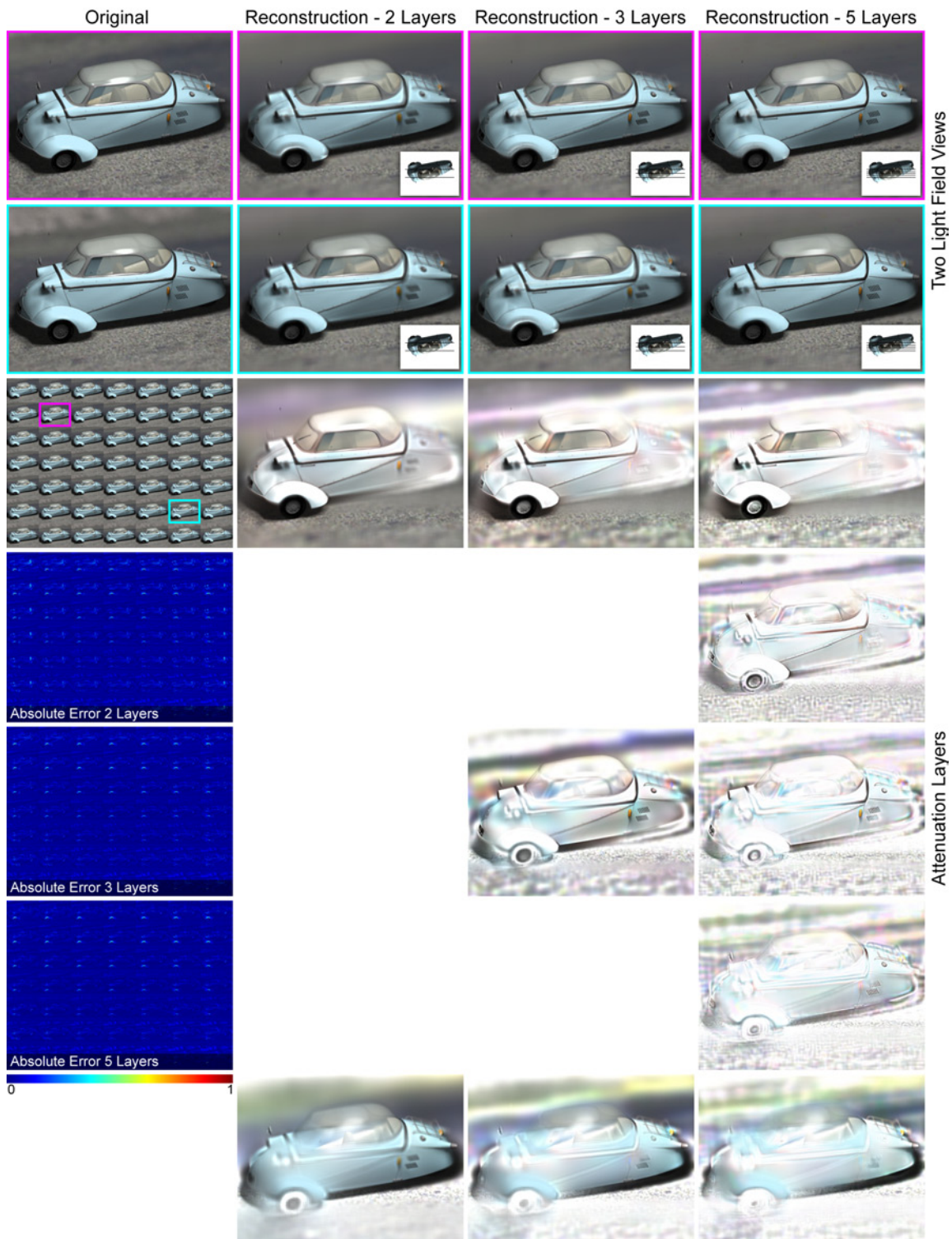
Figure S.2: *The upper two rows show a pair of views from the car light field and simulated reconstructions with two, three, and five attenuation layers; the computed layers are shown underneath in the second, third, and fourth columns, respectively. The light field has a resolution of $384 \times 512 \times 7 \times 7$ samples and covers a field of view of 10°. The layers are equally separated with a depth range of 1/2", which corresponds to four 1/8" plexiglass sheets. The absolute error is shown in the left column, indicating artifacts tend to concentrate at steeper viewing angles.*

| Original | Reconstruction - 2 Layers | Reconstruction - 3 Layers | Reconstruction - 5 Layers |

Two Light Field Views

Attenuation Layers
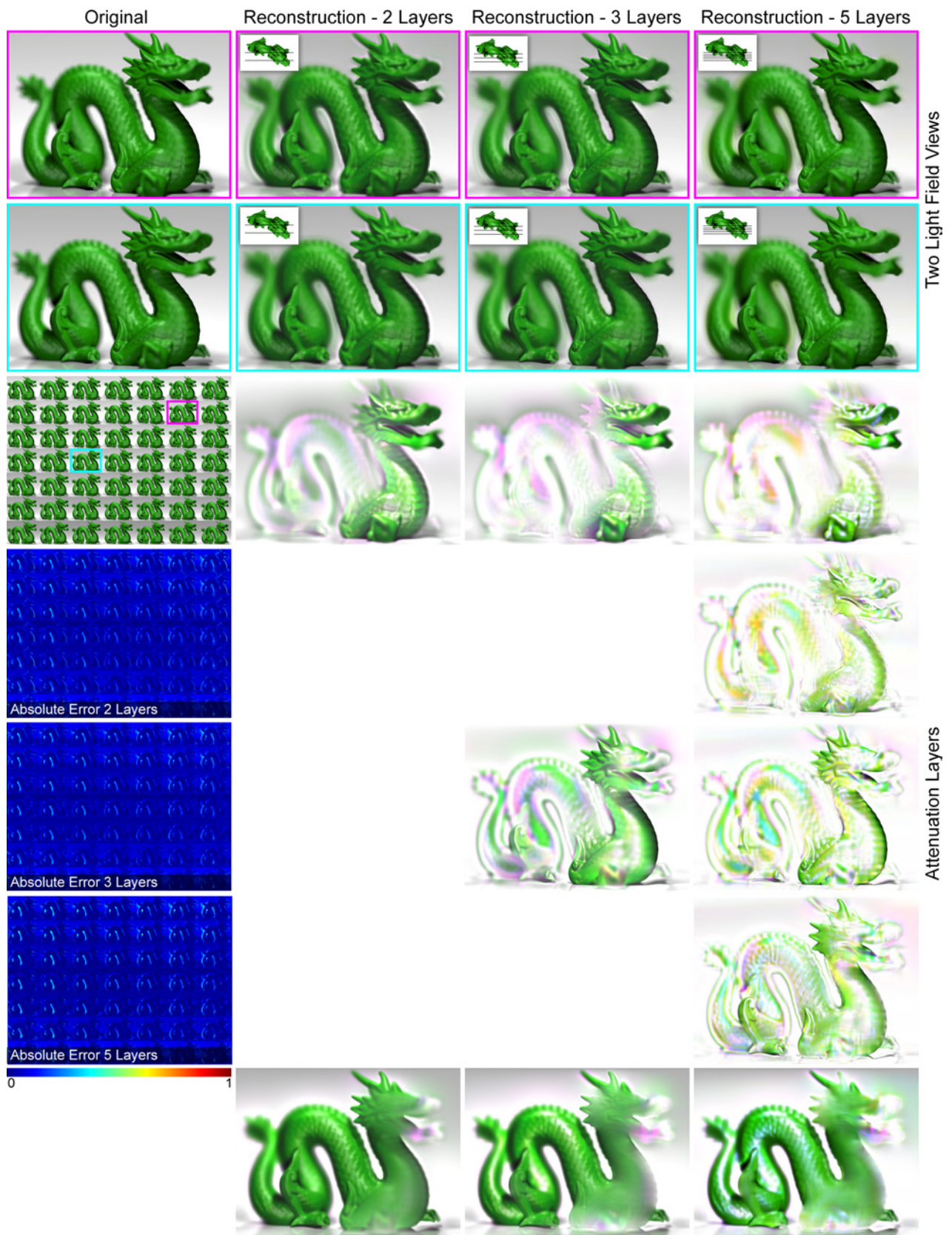
Figure S.3: *Additional results and layer decompositions for the dragon scene with the same parameters as the car.*
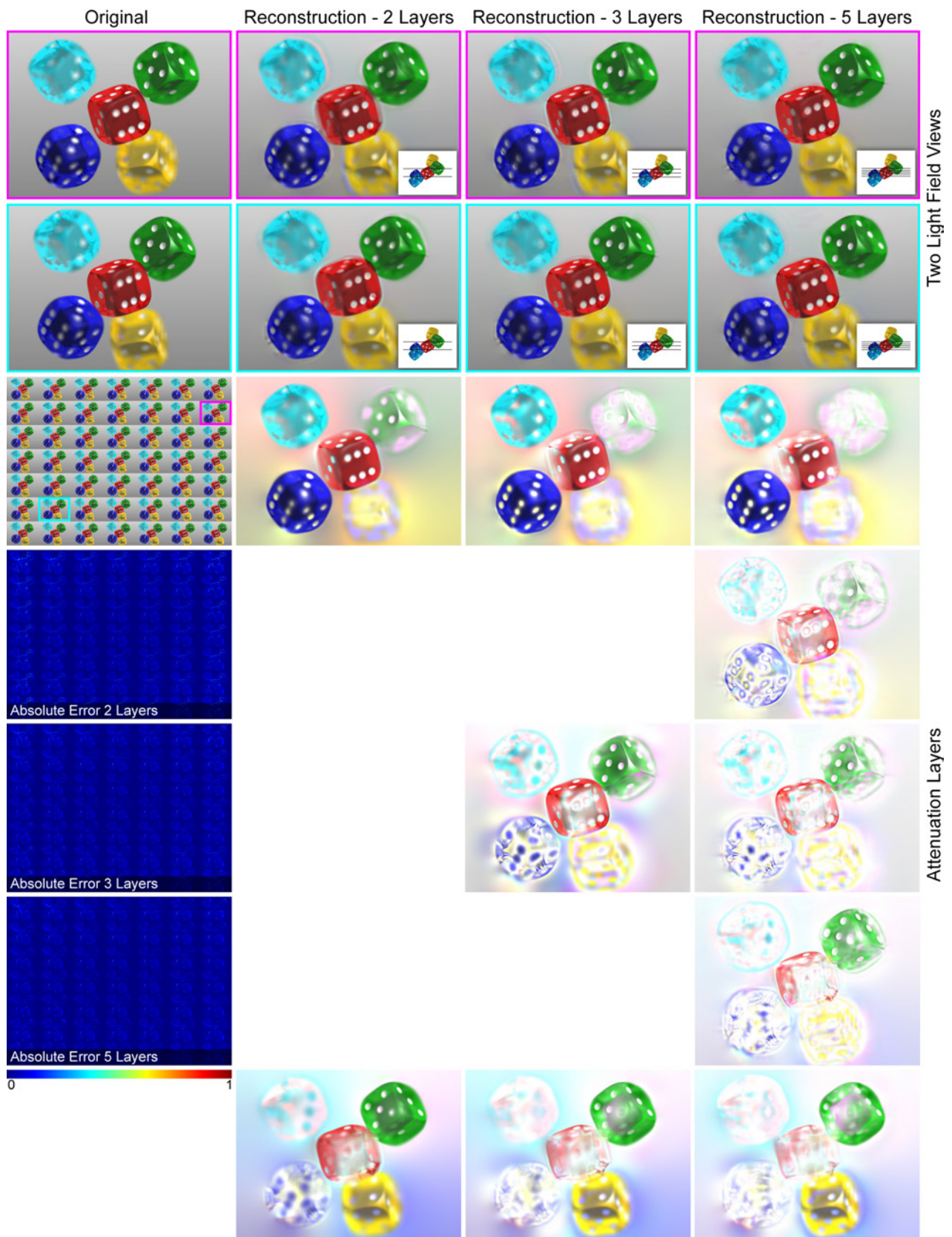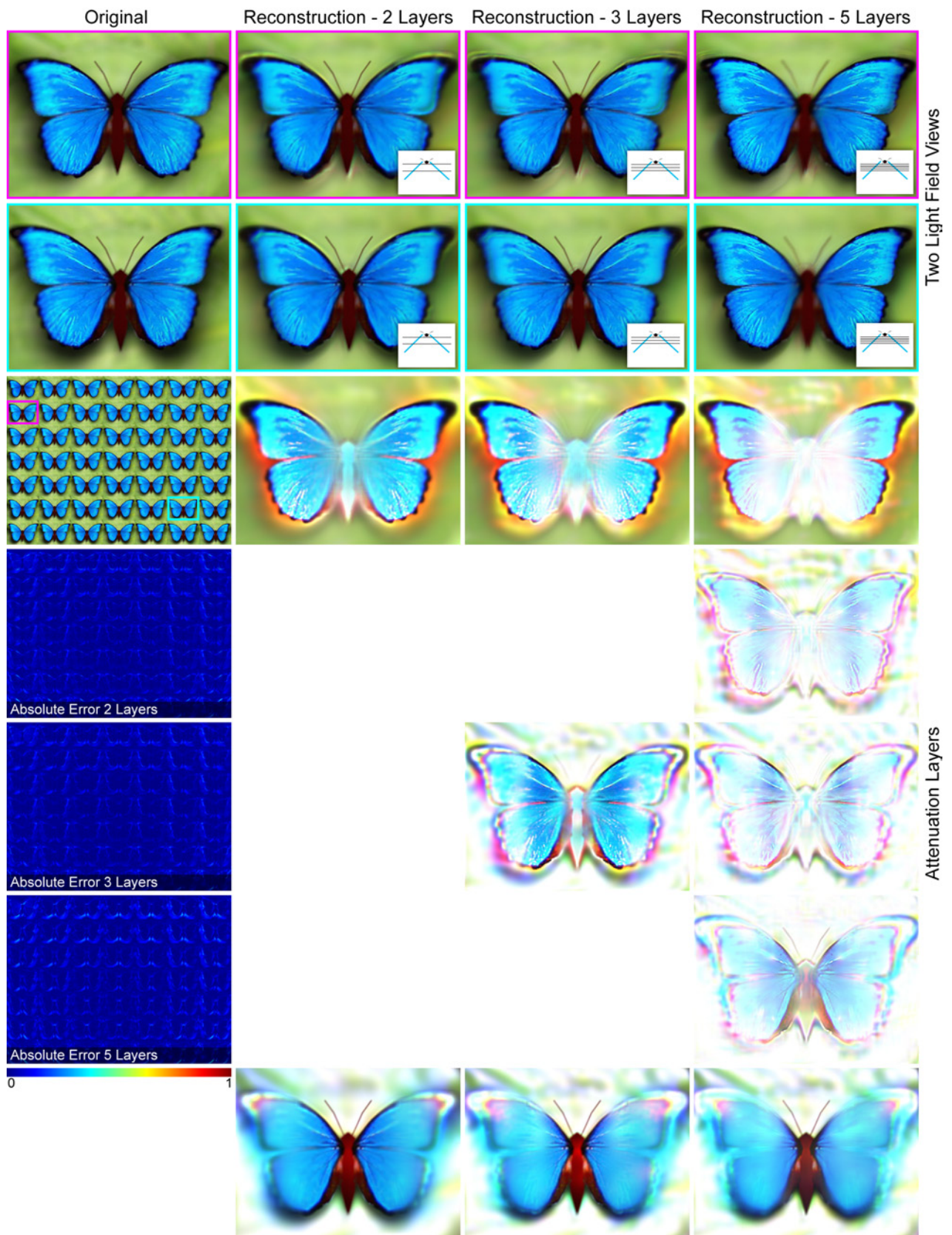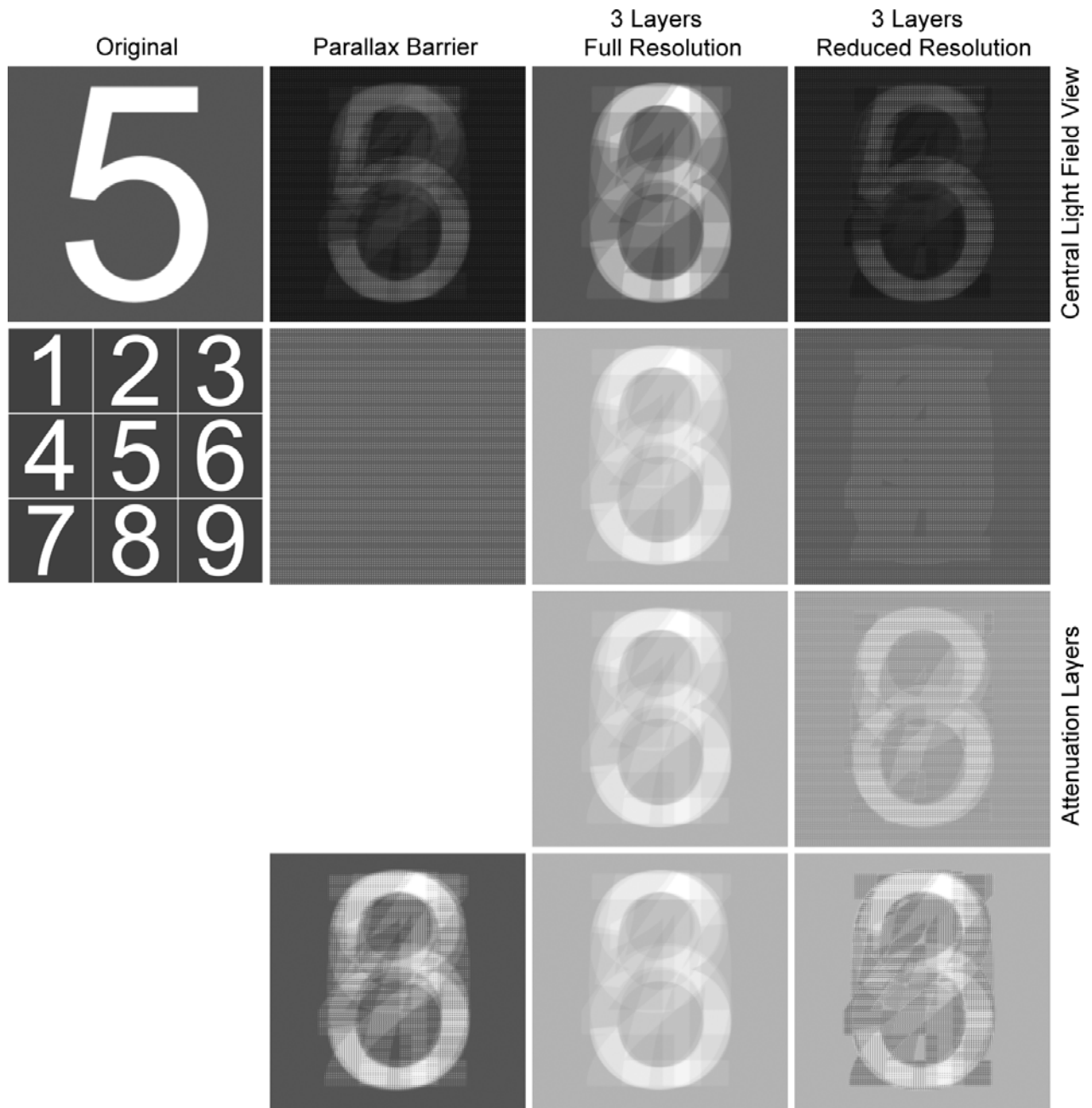
3

Figure S.4: *Additional results and layer decompositions for the dice scene with the same parameters as the car.*

Figure S.5: *Additional results and layer decompositions for the butterfly scene with the same parameters as the car.*

Figure S.6: *Additional results and layer decompositions for the numbers scene. Parallax barrier displays can synthesize arbitrary views, such as the number five, at a reduced spatial resolution (second column). To highlight a common problem of these displays, being limited contrast, the contrast of each layer is simulated to be 4:1 in all examples. An attempt to synthesize this light field at the full spatial resolution, using our tomographic approach for the same overall display thickness, fails (third column). At the same sub-sampling rate, however, the tomographic solution creates attenuation patterns that are similar to those of parallax barrier systems, but also increase contrast in a content-adaptive manner (fourth column). Thus, a similar image resolution as parallax barriers, but with increased contrast, can be achieved for this case (i.e., flip animations) using multiple, disjoint attenuation layers.*

C Additional Results for High Dynamic Range Image Display
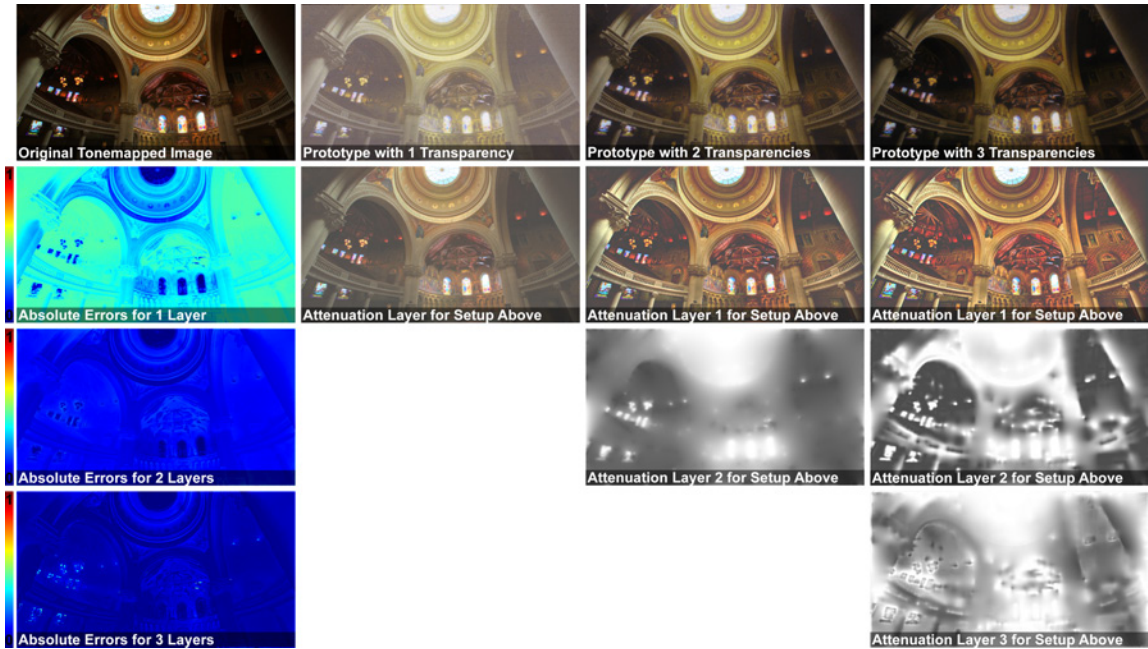
Figure S.7: *Expanded results for multi-layer high dynamic range image display. The first row shows the desired high-contrast image, together with photographs of stacked printed transparencies placed on a light box. From left to right, the physical prototype configuration consists of a single transparency (second column), two transparencies separated by a $1/8$" plexiglass spacer (third column), and three transparencies with $1/8$" plexiglass spacers between each (fourth column). Although overall contrast increases, accurately displaying high-frequency details over a $10°$ field of view at high-contrast is problematic; for example, as seen around the left-most windows in the absolute error plots in the left column, artifacts occur even with multiple layers. The computed attenuation layers are shown underneath each photograph. Note that layers are optimized subject to the black level of the printer.*
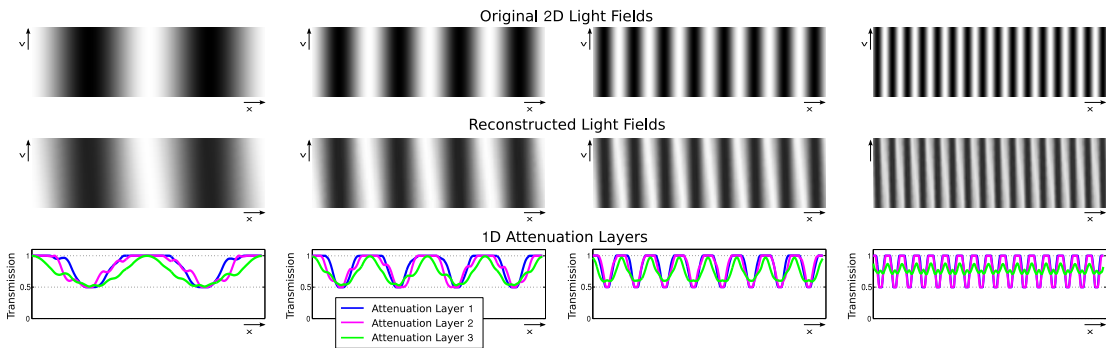

Figure S.8: *Additional analysis of the modulation transfer function. Multiple 2D light fields, containing different spatial frequencies at a high contrast, are shown in the top row. Light fields are parameterized with the spatial coordinate x on the front-most attenuation layer. The local linear angle $v = \tan(\theta)$ gives the relative distance along on a plane at unit distance from the x-axis. The light fields are generated to contain only spatial variation along the x-axis and correspond to desired 1D image frequencies appearing on the front layer. A reconstruction for three disjoint layers, each having a limited contrast of 2:1, is shown in the center row. The corresponding optimized 1D layers are shown along the bottom row. Note that, although high contrast can be reproduced for lower spatial frequencies, it becomes more challenging as the spatial frequency increases. The average difference in contrast between reconstructed and target light field for these examples provides the data for the modulation transfer function shown in Figure 11 in the manuscript and highlights that MTF is computed for a fixed display thickness.*
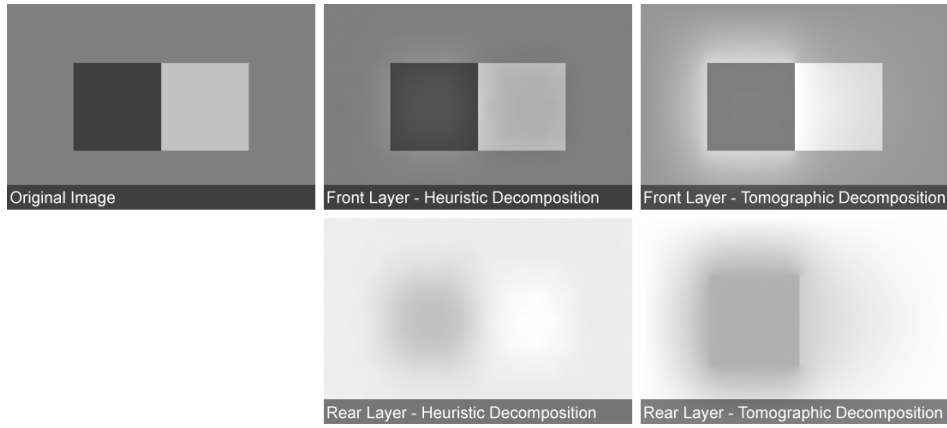
Figure S.9: *Additional results for comparison between existing dual-layer HDR display decompositions [Seetzen et al. 2004] (center) and our tomographic decomposition (right) for a test pattern (left). The front layer is sharpened in both approaches, while the rear layers displays a blurred version of the target image.*

D   Additional Analysis of Display Parameter Optimization
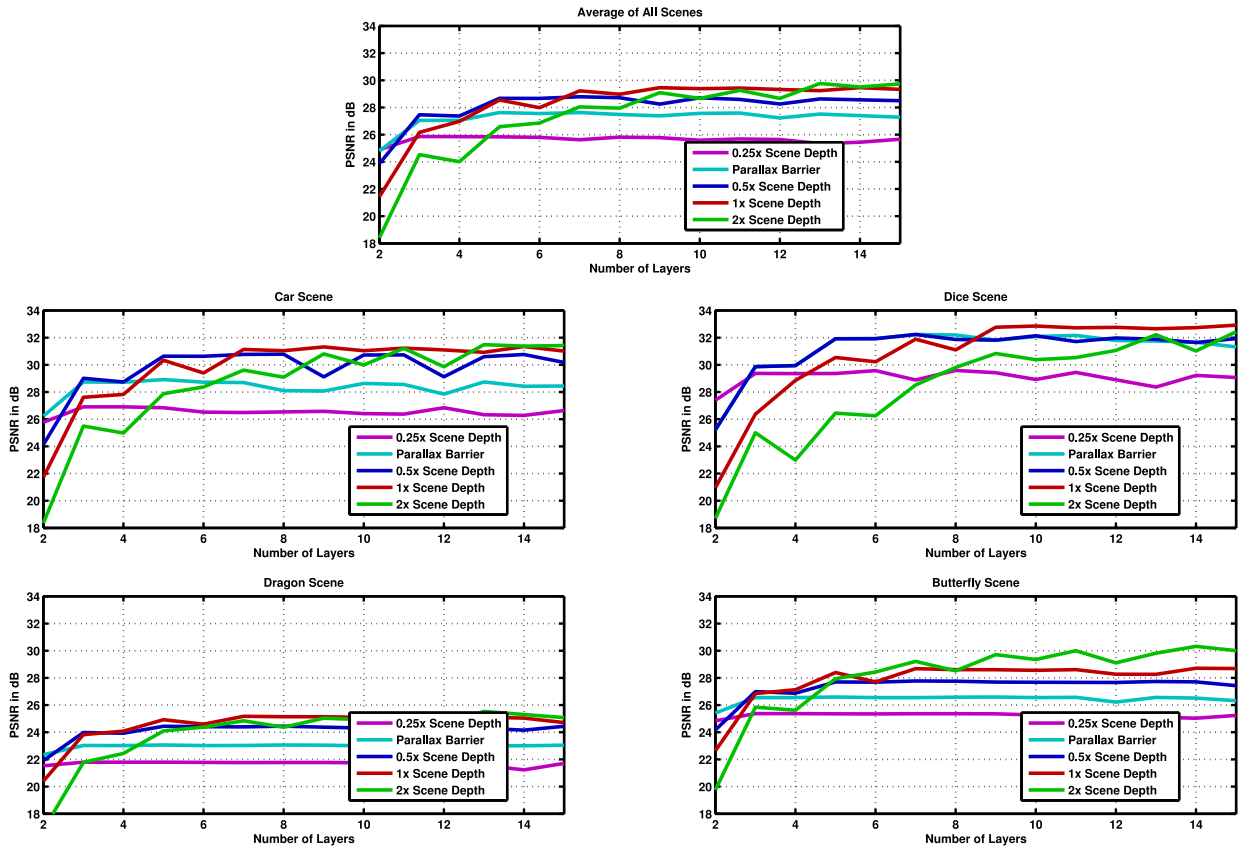
Figure S.10: *Individual plots for all scenes showing the PSNR for an increasing number of layers and display thicknesses. The average performance over all scenes (top) is also shown in Figure 8 in the primary text. In general, the performance is best with a display thickness that is close to that of the virtual scene with a sufficient number of intermediate layers. In practice, the performance is scene-dependent and in most cases, a good reconstruction is achieved with a display thickness that is approximately half of the scene depth or even less. Few layers with a large spacing in between the layers yields poor image quality.*

E   Depth of Field for Multi-Layer Displays

This supplementary appendix provides an extended analysis of the depth of field for multi-layer displays, expanding on Section 4.2 of the primary text. We begin by deriving the upper bound on the spatio-angular bandwidth of any multi-layer, attenuation-based display by applying the central limit theorem to interpret repeated convolutions of mask spectra. This upper bound is shown, for two layers, to encompass prior depth of field expressions for parallax barriers and integral imaging [Moller and Travis 2005; Zwicker et al. 2006]. However, as demonstrated in Section 4 and observed by Gotoda [2010], tomographic decompositions cannot depict all spatio-angular frequencies with equal fidelity—indicating a depth of field more akin to parallax barriers far from the display. We conclude by analyzing the statistical properties of multi-layer displays, again via repeated convolutions, to characterize the expected depth of field. This expression is consistent with existing automultiscopic displays, exhibiting a spatial cutoff frequency inversely proportional to the distance of a virtual surface from the display. Yet, as demonstrated in the primary text, both the upper bound and expected depth of field indicate multi-layer displays can significantly increase the spatial resolution for virtual objects located close to the display surface, as compared to current architectures.

E.1   Depth of Field for Conventional Automultiscopic Displays

As described by Zwicker et al. [2006], the *depth of field* of an automultiscopic display is an expression describing the maximum spatial frequency that can be depicted, without aliasing, in a virtual plane oriented parallel to, and located a known distance from, the display surface. As established in that work, the depth of field can be assessed by analyzing the spectral properties of the displayed light field. For conventional parallax barriers and integral imaging, the discrete sampling of emitted rays (u, a) produces a light field spectrum $\hat{l}(f_u, f_a)$ that is non-zero only within a rectangle. As described by Chai et al. [2000] and Durand et al. [2005], the spectrum of a Lambertian surface, located a distance d_o from the middle of the display, corresponds to the line $f_a = (d_o/d_r)f_u$ in the frequency domain, where d_r is the distance between the u-axis and s-axis, following Figure 3 in Section 3. The spatial cutoff frequency is given by the intersection of this line with the spectral bandwidth of the display. To summarize, conventional automultiscopic displays have a finite depth of field such that the spatial frequency f_ξ in a plane at d_o must satisfy

$$|f_\xi| \leq \begin{cases} \dfrac{f_0}{N_a}, & \text{for } |d_o| + (h/2) \leq N_a h \\[2mm] \left(\dfrac{h}{(h/2)+|d_o|} \right) f_0, & \text{otherwise,} \end{cases} \tag{S.1}$$

where N_a is the number of angular views, h is the thickness of the display, and $f_0 = 1/2p$ is the spatial cutoff frequency of a mask layer with a pixel size of p.

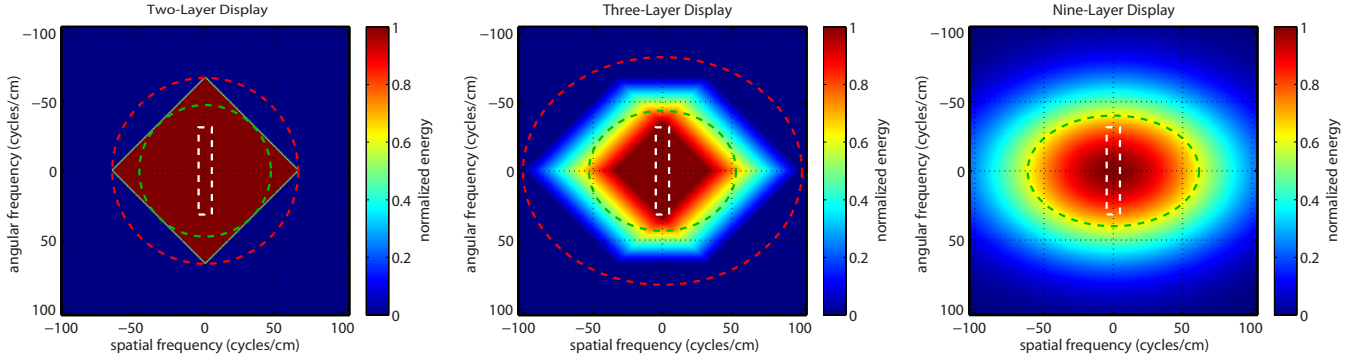## E.2   Upper Bound on Depth of Field for Multi-Layer Displays

The upper bound on the depth of field for a multi-layer display is similarly assessed by considering the maximum spectral bandwidth. It is shown in Section 3.3 that the light field $l(u, a)$ emitted by a multi-layer display is given by

$$l(u, a) = l_0(u, a) \prod_{k=1}^{N_l} t_k(u + (d_k/d_r)a), \tag{S.2}$$

where $l_0(u, a)$ is the backlight profile and $t_k(\xi)$ is the transmittance of mask k. In this appendix the backlight is assumed to be uniform, such that $l_0(u, a) = 1$, and the target light field is normalized such that $l(u, a) \in (0, 1]$. Without loss of generality, it is also assumed that the mask layers are uniformly distributed such that $d_k \in [-h/2, h/2]$. The light field spectrum $\hat{l}(f_u, f_a)$ is given by the two-dimensional Fourier transform of Equation S.2, as follows.

$$\hat{l}(f_u, f_a) = \int_{-\infty}^{\infty} \int_{-\infty}^{\infty} \prod_{k=1}^{N_l} t_k(u + (d_k/d_r)a)\, e^{-2\pi j f_u u}\, e^{-2\pi j f_a a}\, du\, da \tag{S.3}$$

By the convolution property of Fourier transforms [Bracewell 1999], this expression reduces to a *repeated convolution* of the individual mask spectra $\hat{t}_k(f_\xi)$, such that the light field spectrum is given by

Figure S.11: *Upper bound on the depth of field for multi-layer displays. From left to right, the spectral support is illustrated for two-layer, three-layer, and nine-layer displays, evaluated using Equations S.4 and S.5. The system parameters correspond with the prototype described in Section 4 of the primary text, with the parameterization variable $d_r = h/2$. Note that, following Equation S.12, the expected bandwidth of an N_l-layer display converges to a bivariate Gaussian distribution for large N_l. Following Equation S.14, the ellipse corresponding to the upper bound on achievable spatio-angular frequencies is denoted by a dashed red line. The ellipse corresponding to the expected depth of field, as given by Equation S.15, is indicated by a dashed green line. Note that both estimates of the depth of field exceed the bandwidth of conventional automultiscopic displays, shown as a dashed white line.*

$$\hat{l}(f_u, f_a) = \bigotimes_{k=1}^{N_l} \hat{t}_k(f_u)\,\delta(f_a - (d_k/d_r)f_u) = \hat{t}_1(f_u)\,\delta(f_a - (d_1/d_r)f_u) \otimes \cdots \otimes \hat{t}_{N_l}(f_u)\,\delta(f_a - (d_{N_l}/d_r)f_u), \quad \text{(S.4)}$$

where $\bigotimes$ denotes the repeated convolution operator. Note that each mask produces a spectrum $\hat{t}_k(f_u, f_a)$ that lies along a slanted line, following Chai at al. [2000]. Since each mask has a finite resolution, the individual spectra may be non-zero only for $|f_u| \leq f_0$. Thus, we define the maximum spectral bandwidth of any given mask as follows.

$$\hat{t}_k(f_u, f_a) \triangleq \begin{cases} \frac{1}{2\epsilon f_0}, & \text{for } |f_u| \leq f_0 \text{ and } |f_a - (d_k/d_r)f_u| \leq \frac{\epsilon}{2} \\ 0, & \text{otherwise} \end{cases} \quad \text{(S.5)}$$

This definition corresponds to a thin mask with a spatially-varying opacity characterized by a white noise process (i.e., a uniform spectral energy density) [Haykin 2000]. Note that, as derived by Chai et al. [2000], the spectrum of a mask at d_k will be non-zero along a single line, with slope d_k/d_r, only in the limit as ϵ tends to zero.

E.2.1 Two-Layer Displays

For a fixed number of layers, the depth of field can be algebraically or geometrically constructed directly by substituting Equation S.5 into Equation S.4. Note that, for the purposes of deriving an upper bound, the specific form of Equation S.5 is immaterial—only the limited spectral extent is considered. For example, consider the case of two masks, separated by a distance h. The emitted light field spectrum is given by

$$\hat{l}(f_u, f_a) = \hat{t}_1(f_u)\,\delta(f_a - (h/(2d_r))f_u) \otimes \hat{t}_2(f_u)\,\delta(f_a + (h/(2d_r))f_u) \quad \text{(S.6)}$$

As shown in Figure S.11, this gives a diamond-shaped region enclosing the non-zero spectral support of any two-layer display. Following the approach of Zwicker et al. [2006], the spatial cutoff frequency f_ξ is again found by intersecting the line $f_a = (d_o/d_r)f_u$ with the boundary of the maximum-achievable spectral support. This geometric construction yields the following upper bound on the depth of field for any two-layer, attenuation-based display.

$$|f_\xi| \leq \left(\frac{h}{(h/2) + |d_o|} \right) f_0 \quad \text{(S.7)}$$

Comparing Equations S.1 and S.7 reveals the benefits of non-heuristically-constructed two-layer displays. For a fixed display thickness h, we conclude that conventional parallax barriers and integral imaging achieve the maximum spatial resolution far from the display. However, the resolution close to the display is reduced, by a factor up to N_a (i.e., the number of angular views), compared to the upper bound. Thus, conventional fixed spatio-angular resolution tradeoffs [Georgiev et al. 2006] compromise resolution for virtual objects near the display. In comparison, our multi-layer tomographic decomposition is capable of locally varying the spatio-angular resolution tradeoff; as demonstrated in the primary text, this allows accurate depiction of virtual objects at the full mask resolution near the display, while exhibiting a depth of field similar to conventional methods far from the display.

E.2.2 Multi-Layer Displays

The upper bound for an arbitrary number of layers can be assessed using similar methods. Figure S.11 shows the geometric construction of the spectral support for a three-layer display, composed of masks at $d_1 = -h/2$, $d_2 = 0$, and $d_3 = h/2$. The resulting depth of field is given by the following expression.

$$|f_\xi| \leq \begin{cases} \left(\frac{3h/2}{(h/2)+|d_o|}\right) f_0, & \text{for } |d_o| \leq h \\ \left(\frac{h}{|d_o|}\right) f_0, & \text{otherwise} \end{cases}$$

(S.8)

Thus, the display bandwidth exceeds conventional two-layer architectures, motivating the development of multi-layer decompositions for enhanced 3D display. At this point, one may proceed to construct a tight upper bound for any number of layers. However, this construction becomes geometrically cumbersome. Instead, we apply the central limit theorem [Peebles 2000] to obtain an approximate expression for the spectral support due to the repeated convolutions in Equation S.4; as derived by Chaudhury et al. [2010], the repeated convolution of N_l two-dimensional spectra, each with mean $\mu_k = [0,0]$ and covariance matrix $\mathbf{\Sigma}_k$, tends to a bivariate Gaussian distribution, such that

$$\hat{l}(f_u, f_a) \approx \left(\frac{1}{2\pi|\mathbf{\Sigma}|^{\frac{1}{2}}}\right) \exp\left(-\frac{1}{2}\mathbf{f}^\top \mathbf{\Sigma}^{-1}\mathbf{f}\right), \text{ for } \mathbf{\Sigma} = \sum_{k=1}^{N_l} \mathbf{\Sigma}_k,$$

(S.9)

where $\mathbf{f} = [f_u, f_a]$ is a given spatio-angular frequency. The cumulative mean spatio-angular frequency $\mu = \mu_k = 0$, since each mask spectrum is symmetric about the origin as defined in Equation S.5. The covariance matrix for each mask is given by substituting Equation S.5, such that

$$\lim_{\epsilon \to 0} \mathbf{\Sigma}_k = \lim_{\epsilon \to 0} \begin{bmatrix} \int_{-\infty}^{\infty}\int_{-\infty}^{\infty} f_u^2\, \hat{t}_k(f_u, f_a)\, df_u\, df_a & \int_{-\infty}^{\infty}\int_{-\infty}^{\infty} f_u f_a\, \hat{t}_k(f_u, f_a)\, df_u\, df_a \\ \int_{-\infty}^{\infty}\int_{-\infty}^{\infty} f_u f_a\, \hat{t}_k(f_u, f_a)\, df_u\, df_a & \int_{-\infty}^{\infty}\int_{-\infty}^{\infty} f_a^2\, \hat{t}_k(f_u, f_a)\, df_u\, df_a \end{bmatrix} = \frac{f_0^2}{3}\begin{bmatrix} 1 & \frac{d_k}{d_r} \\ \frac{d_k}{d_r} & \left(\frac{d_k}{d_r}\right)^2 \end{bmatrix},$$

(S.10)

where the limit of ϵ tending to zero corresponds to an infinitesimally-thin mask. Thus, the cumulative covariance matrix of the emitted light field spectrum is approximated by the summation

$$\mathbf{\Sigma} = \sum_{k=1}^{N_l} \mathbf{\Sigma}_k = \begin{bmatrix} \sigma_{f_u}^2 & 0 \\ 0 & \sigma_{f_a}^2 \end{bmatrix} = \frac{f_0^2}{3}\begin{bmatrix} N_l & 0 \\ 0 & \left(\frac{N_l(N_l+1)}{12(N_l-1)}\right)\left(\frac{h}{d_r}\right)^2 \end{bmatrix},$$

(S.11)

for masks uniformly-spaced on the interval $d_k \in [-h/2, h/2]$. Substituting into Equation S.9 yields the following approximation for the expected spectrum of an N_l-layer display.

$$\hat{l}(f_u, f_a) \approx \left(\frac{1}{2\pi\sigma_{f_u}\sigma_{f_a}}\right) \exp\left(-\frac{f_u^2}{2\sigma_{f_u}^2} - \frac{f_a^2}{2\sigma_{f_a}^2}\right)$$

(S.12)

In the remainder of this appendix, this expression is used to characterize both the upper bound and the expected depth of field, as depending on the number of layers N_l, display thickness h, and mask cutoff frequency $f_0 = 1/2p$.

11
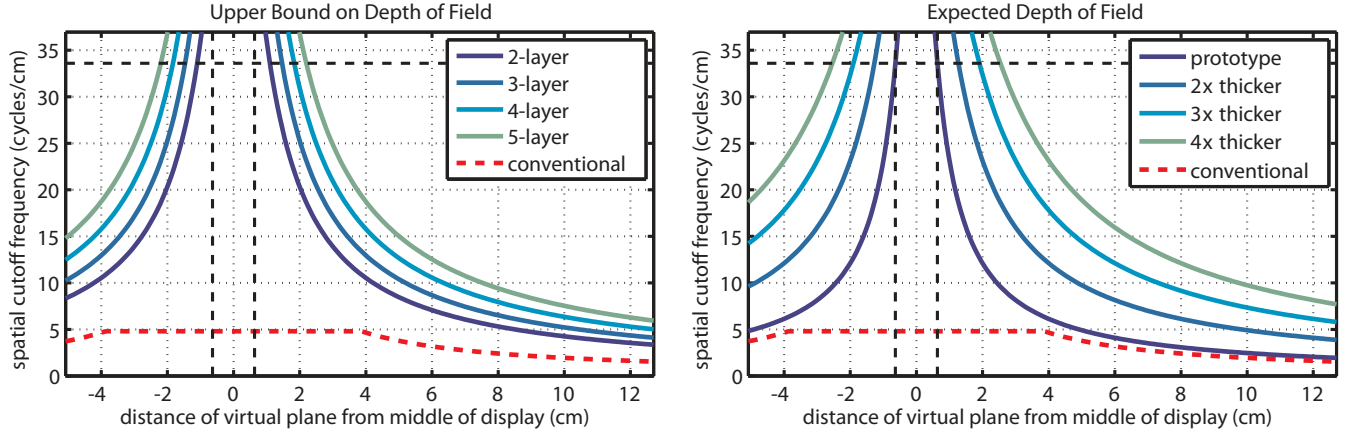
Figure S.12: *Comparing the upper bound to the expected depth of field for multi-layer displays. (Left) The upper bound on the achievable spatio-angular frequencies, as given by Equation S.14. (Right) The expected depth of field, as given by Equation S.16. Note that the expected spatial resolution for our prototype exceeds that of a comparable parallax barrier or integral imaging architecture, as given by Equation S.1, particularly close to the display surface. Increasing the thickness of the display extends the depth of field, both within the display enclosure, as well as beyond its surface. In both figures, the horizontal dashed black line denotes the maximum spatial frequency f_0 for an individual mask. Dashed vertical lines denote the display extent (i.e., $|d_o| \leq h/2$). Display parameters correspond to those for the prototype described in Section 4 of the primary text.*

As shown in Figure S.11, the average spectral support of a multi-layer display is a bivariate Gaussian. Note that curves defining spatio-angular frequencies with equal expected modulation energies correspond to ellipses, such that

$$\frac{f_u^2}{\sigma_{f_u}^2} + \frac{f_a^2}{\sigma_{f_a}^2} = \lambda^2, \tag{S.13}$$

where $\pm\lambda\sigma_{f_u}$ and $\pm\lambda\sigma_{f_a}$ are the points of intersection with the f_u-axis and f_a-axis, respectively. At this point, one can obtain an approximate upper bound on the depth of field, for an arbitrary number of layers, by finding the intersection of the line $f_a = (d_o/d_r)f_u$ with the ellipse corresponding to the highest spatial frequency achievable by an N_l-layer display. From Equations S.4 and S.5, the repeated convolution of N_l masks, each extending over $\pm f_0$ along the f_u-axis, will produce non-zero spatial frequencies within the region $|f_u| \leq N_l f_0$. Thus, the ellipse with $\lambda = N_l f_0/\sigma_{f_u}$ provides the following approximate upper bound on the depth of field for an N_l-layer display.

$$|f_\xi| \leq N_l f_0 \sqrt{\frac{(N_l+1)h^2}{(N_l+1)h^2 + 12(N_l-1)d_o^2}} \tag{S.14}$$

This expression approximates the depth of field for two-layer and three-layer displays, given exactly by Equations S.7 and S.8, respectively. A comparison of the upper bound for multi-layer vs. conventional automultiscopic displays is shown in Figure S.12. Note that additional layers significantly increase the upper bound on the achievable spatial resolution, which is expected due to repeated convolution of individual mask spectra via Equation S.4.

E.3 Expected Depth of Field for Multi-Layer Displays

While the upper bound in Equation S.14 indicates the potential of multi-layer displays to significantly increase the spatio-angular resolution of automultiscopic displays, such dramatic gains do not appear to be realized in practice. As described in Sections 4 and 7 of the main text, attempting to replicate a spatial frequency $|f_\xi| > f_0$ (i.e., higher than the Nyquist rate allowed by the mask pixels), especially in a plane far from the display, leads to significant blurring and reconstruction artifacts. Thus, we desire a more conservative estimate of the depth of field practically

achievable with multi-layer displays. In this section we consider the statistical properties of multi-layer displays to characterize an expected depth of field consistent with experiments presented in the primary text.

As shown in Figure S.11, the expected energy spectrum of a multi-layer display containing masks with random opacity is a bivariate Gaussian distribution. We observe that the expected modulation energies, for spatio-angular frequencies near the upper bound ellipse given by $\lambda = N_l f_0 / \sigma_{f_u}$ in Equation S.13, approach zero. Thus, while such spatio-angular frequencies are feasible, significant energy cannot be delivered within this range. However, for spatio-angular frequencies closer to the origin, the expected modulation energy increases. This observation is used to derive an *expected depth of field* expression for multi-layer, attenuation-based displays.

We assume that a display designer will not attempt to exceed the spatial resolution physically achievable on the outer mask layer (i.e., $|f_\xi| \leq f_0$). If this is the case, then one can define the expected depth of field as the set of spatio-angular frequencies that, on average, can be modulated with energies equivalent to that achieved for a sinusoid with a spatial frequency $f_0 = 1/2p$ rendered on the display surface. Thus, we substitute $\lambda = \sqrt{6(2N_l - 1)/(N_l(N_l + 1))}$ into Equation S.13 such that the depth of field satisfies $|f_\xi| \leq f_0$ in a plane located at $d_o = h/2$ from the middle of the display. This yields the following expected depth of field expression.

$$|f_\xi| \leq f_0 \sqrt{\frac{2(2N_l - 1)h^2}{(N_l + 1)h^2 + 12(N_l - 1)d_o^2}} \tag{S.15}$$

Taking the limit as N_l tends to infinity gives the expected depth of field for a volumetric attenuator, as follows.

$$|f_\xi| \leq f_0 \sqrt{\frac{4h^2}{h^2 + 12d_o^2}} \tag{S.16}$$

As shown in Figure S.12, this expression predicts that a multi-layer display can, on average, achieve spatio-angular frequencies exceeding conventional designs, particularly for virtual objects near the display surface or when the thickness h of the display exceeds that of a conventional parallax barrier construction.

In this supplementary appendix, we have provided an upper bound and expected trends for the depth of field of multi-layer displays. From the upper bound it is apparent that the spatio-angular bandwidth of multi-layer displays significantly exceeds conventional two-layer architectures. However, experiments in the primary text confirm a limited depth of field similar to conventional automultiscopic designs. We caution that additional theoretical work is required to fully quantify such displays, yet we believe our upper bound and expected depth of field do provide a solid intuition: multi-layer displays exhibit a finite depth of field, similar to existing automultiscopic designs, wherein the resolution far from the display falls as $|f_\xi| \leq \gamma(h/|d_o|)f_0$, where γ is a proportionality constant that depends on the system architecture (e.g., $\gamma = 1/\sqrt{3}$ for multi-layer displays via Equation S.16). This trend is used in Section 4 to motivate the manual construction of an approximate display prefilter, similar to Zwicker et al. [2006], wherein the finite depth of field is accounted for by blurring objects as they translate away from the display. Yet, the complex interplay between spatio-angular resolution and reconstruction artifacts for tomographically-optimized multi-layer displays remains a promising direction of research.

Supplementary References

BRACEWELL, R. 1999. *The Fourier Transform and Its Applications (Third Edition)*. McGraw-Hill.

CHAI, J.-X., TONG, X., CHAN, S.-C., AND SHUM, H.-Y. 2000. Plenoptic sampling. In *ACM SIGGRAPH*, 307–318.

CHAUDHURY, K. N., MUÑOZ-BARRUTIA, A., AND UNSER, M. 2010. Fast space-variant elliptical filtering using box splines. *IEEE Trans. Image 19*, 9, 2290–2306.

DURAND, F., HOLZSCHUCH, N., SOLER, C., CHAN, E., AND SILLION, F. X. 2005. A frequency analysis of light transport. In *ACM SIGGRAPH*, 1115–1126.

GEORGIEV, T., ZHENG, K. C., CURLESS, B., SALESIN, D., NAYAR, S., AND INTWALA, C. 2006. Spatio-angular resolution tradeoff in integral photography. In *Eurographics Symposium on Rendering*, 263–272.

GOTODA, H. 2010. A multilayer liquid crystal display for autostereoscopic 3D viewing. In *SPIE-IS&T Stereoscopic Displays and Applications XXI*, vol. 7524, 1–8.

HAYKIN, S. 2000. *Communication Systems (Fourth Edition)*. Wiley.

MOLLER, C. N., AND TRAVIS, A. R. L. 2005. Correcting interperspective aliasing in autostereoscopic displays. *IEEE Transactions on Visualization and Computer Graphics 11*, 228–236.

PEEBLES, P. 2000. *Probability, Random Variables, and Random Signal Principles (Fourth Edition)*. McGraw-Hill.

SEETZEN, H., HEIDRICH, W., STUERZLINGER, W., WARD, G., WHITEHEAD, L., TRENTACOSTE, M., GHOSH, A., AND VOROZCOVS, A. 2004. High dynamic range display systems. *ACM Trans. Graph. 23*, 3, 760–768.

ZWICKER, M., MATUSIK, W., DURAND, F., AND PFISTER, H. 2006. Antialiasing for automultiscopic 3D displays. In *Eurographics Symposium on Rendering*.